Carbon dioxide distribution, origins, and transport along a frontal boundary during summer in mid-latitudes

Arkayan Samaddar[1], Sha Feng[1], Thomas Lauvaux[2], Zachary R. Barkley[1], Sandip Pal[3], Kenneth J. Davis[1]

[1]Department of Meteorology and Atmospheric Science, The Pennsylvania State University, University Park, PA 16802, USA.
[2]Laboratoire des Sciences du Climat et de l'Environnement, CEA, CNRS, UVSQ/IPSL, Université Paris-Saclay, Orme des Merisiers, 91191 Gif-sur-Yvette CEDEX, France.
[3]Department of Geosciences, Mail Stop 1053, Texas Tech University, Lubbock, TX 79409, USA

Key Points:

- High resolution simulation of a cold front passage captures the narrow band of elevated CO_2 ahead of the cold front
- CO_2 inflow from the continental boundaries along with biogenic and fossil fuel fluxes create the summertime frontal CO_2 distribution
- Horizontal and vertical advection dominate atmospheric CO_2 transport along the frontal boundary

Corresponding author: Arkayan Samaddar, arkayan@psu.edu

Abstract

Synoptic weather systems are a major driver of spatial gradients in atmospheric CO_2 mole fractions. During frontal passages air masses from different regions meet at the frontal boundary creating significant gradients in CO_2 mole fractions. This study quantitatively describes the atmospheric transport of CO_2 mole fractions during a mid-latitude cold front passage and explores the impact of various sources of CO_2. We focus here on a cold front passage over Lincoln, Nebraska on August 4th, 2016 observed by aircraft during the Atmospheric Carbon and Transport (ACT)-America campaign. A band of air with elevated CO_2 was located along the frontal boundary. Differences in CO_2 across the front were as high as 25 ppm. Numerical simulations using WRF-Chem at cloud resolving resolutions (3km) coupled with CO_2 surface fluxes and boundary conditions from CarbonTracker (CT-NRTv2017x) were performed to explore atmospheric transport at the front. Model results demonstrate that the frontal CO_2 difference in the upper troposphere can be explained largely by inflow from outside of North America. This difference is modified in the atmospheric boundary layer and lower troposphere by continental surface fluxes, dominated in this case by biogenic and fossil fuel fluxes. Horizontal and vertical advection are found to be responsible for the distribution of CO_2 mole fractions along the frontal boundary. This study highlights the use of high-resolution simulations in capturing CO_2 transport along a frontal boundary.

1 Introduction

Atmospheric CO_2 mole fractions have changed from 280 ppm during the pre-industrial period (circa. 1750) to present day mole fractions of 414 ppm (www.esrl.noaa.gov/gmd/ccgg/trends/). Over the last decade, the rate of increase in global atmospheric CO_2 mole fractions has risen from 1.8 ppm/year in 2008 to 2.4 ppm/year in 2018. These changes in atmospheric CO_2 have been linked to an increase in fossil fuel usage (Edenhofer et al., 2014; Skeie et al., 2011) and land use change (Houghton et al., 2012). About 55% of the CO_2 emissions are currently absorbed into oceans or terrestrial ecosystems (Le Quéré et al., 2017).In order to close the budget of atmospheric CO_2, the driving mechanisms of sources and sinks of CO_2 from continental surfaces and oceans need to be better quantified (Le Quéré et al., 2017). Studies have shown that northern hemisphere terrestrial ecosystems are a significant part of the terrestrial sink (Denning et al., 1995; Tans et al., 1990). However, uncertainties in these estimates exist due to lack of knowledge regarding primary drivers of the land sink (Huntzinger et al., 2017). Peylin et al. (2002) and Xiao et al. (2014) show that one of the key uncertainties in regional carbon flux estimates comes from errors in representation of atmospheric transport.

Atmospheric transport models are used to determine sources and sinks of CO_2 through the process of inversion – linking CO_2 mole fractions in the atmosphere to sources and sinks at the surface (Enting et al., 1995). Atmospheric transport models need to be accurate and precise in order to infer CO_2 sources and sinks with accuracy (Gurney et al., 2002). Comparing the transport models to the measurements from the CO_2 observation help determine the uncertainty in the ability of the models in reproducing the carbon cycle (Friedlingstein & Prentice, 2010). While significant progress has been made in understanding the global carbon cycle and its drivers, due to the misrepresentation of transport processes in numerical models, there are gaps in linking anthropogenic CO_2 emissions to rising atmospheric CO_2 mole fractions (Le Quéré et al., 2009). Differences in the representation of transport processes within numerical models lead to biased representation of CO_2 at a global scale (Schuh et al., 2019). Numerical models running at synoptic scale resolutions represent mesoscale and microscale weather events through parameterizations of physical transport processes (Carvalho et al., 2014).

Synoptic scale events like frontal passages play an important role in the transport of CO_2 (Parazoo et al., 2008). These events impact atmospheric CO_2 distributions from

regional to global scales. Models suffer from errors in representation of atmospheric transport in numerical models leading to errors in the inverse estimation of CO_2 fluxes (Lauvaux & Davis, 2014; Houweling et al., 2010; Law et al., 1996). Strong gradients in CO_2 mole fractions at frontal boundaries have been captured by both tower measurements (Hurwitz et al., 2004) and aircraft measurements (Pal et al., 2020). Gradients in atmospheric CO_2 mole fractions (simulated and observed) are advected by horizontal winds over large distances (Chan et al., 2004; Corbin & Denning, 2006; Geels et al., 2004), and are impacted by spatial differences in surface fluxes (Miles et al., 2012). Lifting near the frontal boundary and mixing in the boundary layer define the vertical structure in CO_2 distributions over large scales (Parazoo et al., 2008, 2011).

However, these studies (Parazoo et al., 2008, 2011) have been performed on an annual scale using the PCTM global model (Kawa, 2004) driven by coarse resolution weather reanalysis (1.25° x 1° (longitude x latitude)). Multiple frontal passages were studied over a year and the averaged results were reported as a climatology. We performed this study at a higher resolution and is able resolve some cloud convection, which presents a more resolved description of frontal transport. Pal et al. (2020) observed that there are spatial differences as large as 30 ppm (calculated as the difference between mole-fractions in the warm sector and cold sector) in atmospheric CO_2 distributions across cold frontal boundaries. Regional numerical weather models like WRF-Chem (Skamarock et al., 2008) can be used to simulate frontal passages, their impact on CO_2 mole fractions, the causes of the simulated differences in CO_2 and the impact of model resolution on the simulation. In our study, a summer cold front passing over Lincoln, NE, USA is simulated using WRF-Chem v3.6.1. The transport of CO_2 is quantified and broken down into contributions from horizontal and vertical advection and vertical diffusion. In this study, we aim to investigate atmospheric transport interactions with CO_2 mole-fractions from different sources (biosphere, fossil fuel etc.,) during a cold front passage.

We use WRF-Chem, run at 27, 9 and 3-km resolution, to simulate a 4 August 2016 cold frontal passage that was observed during the summer 2016 ACT-America flight campaign. We compute the terms in the CO_2 transport equation at the frontal boundary to compare their importance as a function of resolution, and we evaluate the origin of the CO_2 mole fraction differences simulated at the frontal boundary. Airborne observations are used to evaluate the plausibility of the numerical results.

This study is structured as follows – the data and methods section describe the numerical model and the tools and analysis methods used for this study. The results section characterizes the capabilities of the numerical modeling system and describes the CO_2 distribution along the frontal boundary and its evolution with time. Transport of CO_2 is broken out by terms in the conservation equation, including the impact of model grid-resolution on the representation of CO_2 transport. The final section highlights the implications of this study to the broader scientific community.

2 Data and Numerical Framework

2.1 ACT-America Aircraft Measurements

The Atmospheric Carbon and Transport (ACT)-America mission is a NASA Earth Venture Suborbital mission designed to improve atmospheric inverse estimates of Greenhouse Gas (GHG) fluxes. One objective is to quantify and reduce atmospheric GHG transport uncertainties (Davis et al., 2020). Two aircraft, a NASA Wallops C-130 Hercules and a NASA Langley B200 King Air collected remote and in-situ measurements in the boundary layer and free troposphere. During frontal passages, flight paths were designed to make measurements in both the warm and cold sectors by crossing frontal systems at multiple levels. Multiple vertical profiles were also collected on both sides of the front. In situ CO_2 measurements from the B200 and C-130 aircraft were collected using a PI-

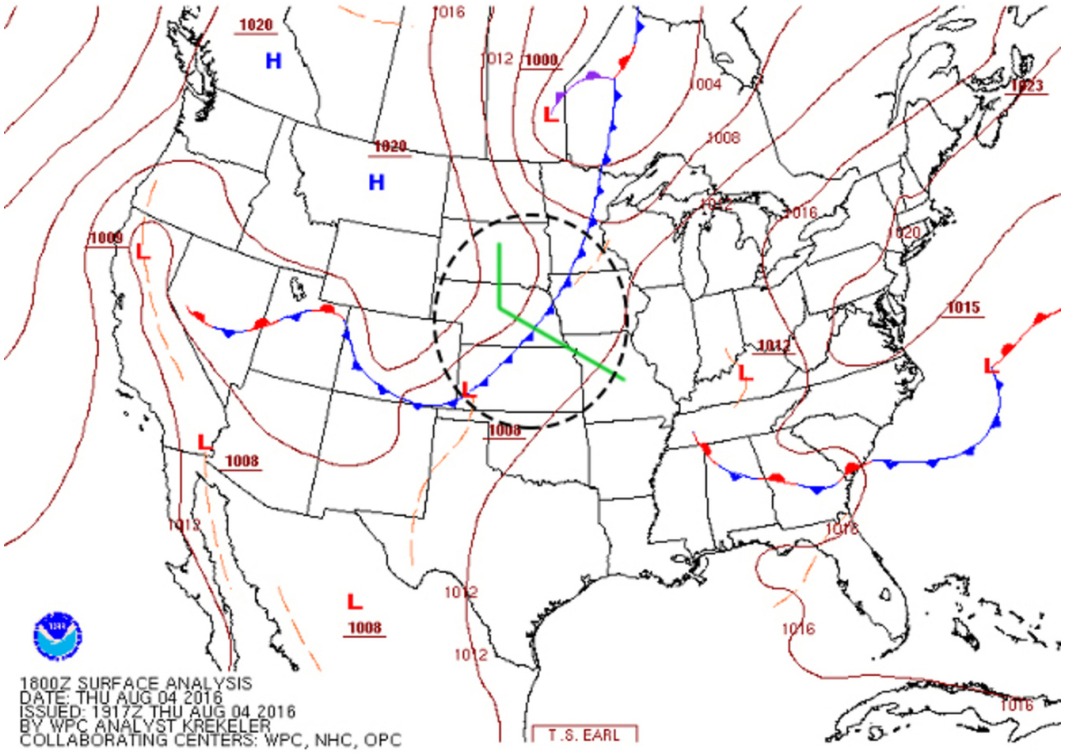

Figure 1. Synoptic map over continental U.S. on August 4th, 2016 at 18Z. The cold front studied is highlighted in the black dashed circle and the green line shows the approximate flight path for the ACT-America aircraft. Courtesy: NOAA/National Weather Service

CARRO 2401-m spectrometer (Digangi et al., 2018) along with atmospheric state variables. Data sets and management are described by Davis et al. (2018). In this study, the performance of the numerical model used was evaluated using in-situ measurements from the ACT-America aircraft on August 4th, 2016.

2.2 Cold front passage on August 4th, 2016

The summer 2016 flight campaign was in the Midwest region of the U.S. from August 1st to August 17th. A cold front crossed south-eastern Nebraska, Iowa and northern Kansas (located within the 3km simulation domain) from August 4th 18Z to August 5th 12 Z. Figure 1 shows the synoptic map for the frontal passage with the flight track overlay. The low-pressure center of the front was located over Manitoba in Canada. The cold front passage was characterized by a 170^o change in wind directions at the frontal boundary - northerly winds to southerly winds. The Lincoln airport station (KLNK) recorded that the daytime mean temperature dropped by 12 K between the 4th and 5th of August. The change in the airmass over the station was also accompanied by a 10% decrease in relative humidity and a 10 hPa drop in surface pressure. To capture the gradients in CO_2 mole fractions across the frontal boundary, the aircraft crossed the front at multiple altitudes (300 m, 3 km, 5 km and 8 km MSL) on August 4th between 16Z and 21Z. Vertical profiles were also taken at multiple locations in the warm and cold sector. The aircraft recorded a 25 ppm change in CO_2 while crossing the frontal boundary in the atmospheric boundary layer (ABL) (Pal et al., 2020).

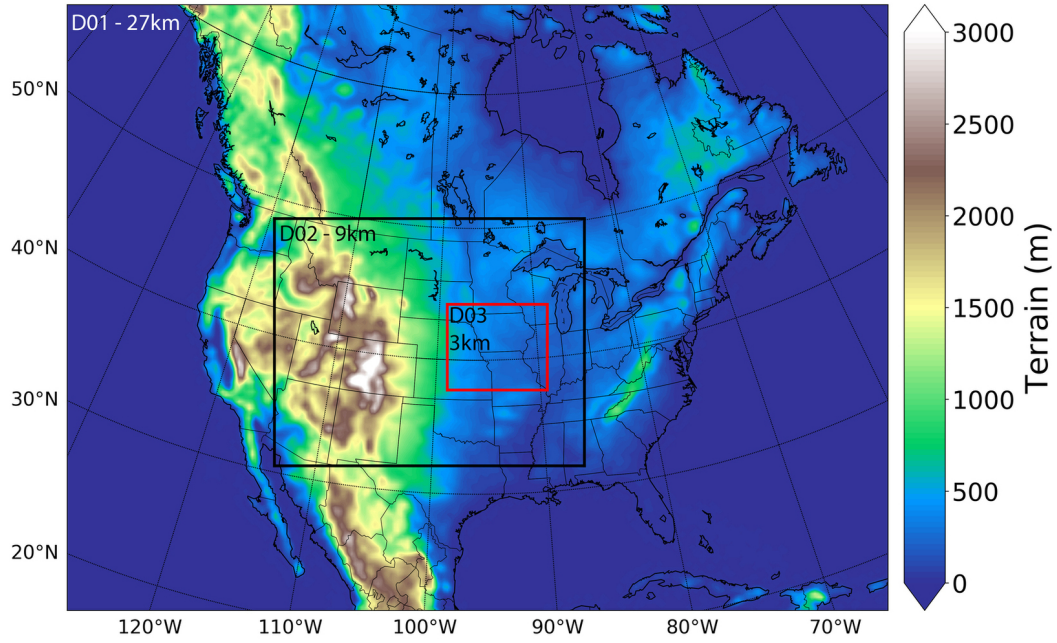

Figure 2. Domains used for the WRF-Chem model simulations, shown with contours of terrain height in meters above sea level. The map shows the 27 km resolution domain (D01), the black inner box shows the 9 km domain (D02) and the innermost red box shows the 3 km domain (D03).

2.3 Model Description

For this study, we use the Weather Research and Forecasting Model with Chemistry - WRF-Chem ver. 3.6.1 (Skamarock et al., 2008). The model was run with one-way nesting via three nested domains with spatial grid resolutions of 27 km, 9 km, and 3 km respectively, using WRF-Chem with a modification to include CO_2 as a passive tracer (Lauvaux et al., 2012). Figure 2 shows the arrangement of the nested domains as used in WRF-Chem. Vertical grid resolution has been kept constant across the domains with 51 terrain-following eta levels from the surface to the top of the atmosphere (at 100hPa). The vertical grids are staggered with 29 levels forming a higher density grid under 2km AGL (above ground level), with greater spacing above. The first vertical level has an elevation of 8 m above ground level.

The simulations were initialized with meteorological driver data from 6-hourly ERA-Interim (Dee et al., 2011) outputs with a reduced Gaussian grid with approximately uniform 79 km spacing for surface and other grid-point fields (Berrisford et al., 2011) and NCEP high-resolution SST data. Model physics are summarized in Table 1. We output WRF-Chem hourly for the period from July to August 2016, in which the model was re-initialized every 5 days and with 12-hour meteorological spin-up.

2.4 CO_2 Simulations

WRF-Chem transport was coupled with CO_2 fluxes from the CarbonTracker Near Real Time v2017 (CT-NRT.v2017) (Peters et al., 2007), hereafter referred to as CarbonTracker. CO_2 is simulated as a passive tracer in this study – similar to setups described in prior studies (Butler et al., 2019; Feng, Lauvaux, Keller, et al., 2019; Feng, Lauvaux, Davis, et al., 2019). CarbonTracker provided surface fluxes as well as lateral boundary

Table 1. Parameterization options used for WRF-Chem simulations

Option	Parameter
Microphysics	Thompson (Thompson et al., 2008)
PBL Scheme	MYNN2 (Nakanishi & Niino, 2006)
Longwave Radiation	RRTMG longwave scheme (Iacono et al., 2008)
Shortwave Radiation	RRTMG shortwave scheme (Iacono et al., 2008)
Land Surface	Unified Noah land-surface model (Chen & Dudhia, 2001)
Cumulus Parameterization	Kain-Fritsch (new Eta) scheme (Kain, 2004), for the 27 km and 9 km resolution domains

conditions. Within the WRF-Chem framework, these surface fluxes are tracked as individual tracers simulating fossil fuel emissions, biogenic fluxes, oceanic fluxes, and biomass burning emissions. CO_2 inflow from CarbonTracker to the boundaries of the WRF-Chem domains are tracked separately as lateral boundary condition tracers with the consideration of CO_2 mass conservation. Horizontal and vertical interpolations were applied using weights based on the pressure level differences between the two models. More details can be found in Butler et al. (2019). Thus, by considering the sum of all the individually traced tracers, the total atmospheric CO_2 mole fractions are determined. The lateral boundary conditions have a $3^\circ \times 2^\circ$ spatial resolution and the set of surface fluxes have a $1^\circ \times 1^\circ$ resolution over the study domain. Temporally, all the fluxes are introduced as 3-hourly mean values. The simulation is initialized with an atmosphere free of CO_2. Lateral boundary conditions along with surface fluxes populate the domain with CO_2 while WRF-Chem transport moves it within the domain. WRF-Chem was run for a month prior to the campaign period (July 2016) to ensure realistic CO_2 mole fractions (approximately 410 ppm) in the domain atmosphere before simulating the study period (August 2016).

2.5 Breakdown of CO_2 mole fractions into components

Within the WRF-Chem framework, the simulated atmospheric CO_2 mole fractions are calculated as the sum of components from CarbonTracker, which are related to the various surface fluxes of CO_2 along with the lateral boundary conditions. By tracking the individual tracers, it is possible to show the interaction between atmospheric transport features created due to the cold front passage and CO_2 emitted from these various sources and the boundary conditions. In this study, the CO_2 from the boundary conditions represent inflow from outside the simulation domains. These interactions can highlight which CO_2 tracer is impacted the most by the frontal passage. Further, a footprint analysis has also been performed to trace the origins of the airmasses at the frontal boundary. Thus, by combining these two analyses it is possible to determine which sources of CO_2 were responsible for the atmospheric distribution during the period of frontal passage.

WRF-Chem was configured to simulate CO_2 originating from fossil fuel, biogenic, oceanic, and fire surface fluxes, and boundary conditions as separate tracers. Due to negligible impacts of oceanic and fire sources on CO_2 during the study period (< 1 ppm), we focus only on fossil fuel, biogenic and boundary condition tracers to investigate how the transport impacts them individually and quantify their contribution to specific features such as the band of elevated CO_2 mole fractions along the frontal boundary.

3 Methods

3.1 Model-Data Comparison

During the ACT-America flight campaign, CO_2 mole fractions along with standard atmospheric variables (potential temperature, water vapor mole fraction etc.) were measured on both aircraft (Davis et al., 2018). Similarly, simulated values of potential temperature and CO_2 mole fractions were extracted from WRF-Chem simulation atmosphere along the flight tracks to evaluate model performance. A limitation in this approach arose from the different time and spatial resolution of the products used. The modeled potential temperature and CO_2 mole fraction values were extracted from nearest points to the observations. The aircraft data are archived with a time resolution of 5 seconds (Davis et al., 2018), while the WRF-Chem setup used has been configured with hourly output. For this evaluation, measurements taken within 30 minutes of a WRF-Chem output were used. In order to compare aircraft measurements along constant altitude flight legs, horizontal maps were extracted from WRF-Chem at the same altitude. A transect drawn almost parallel to the flight path was used to compare the vertical features of the front as described by WRF-Chem and the aircraft measurements.

3.2 Calculating CO_2 transport terms

As mentioned in section 2.4, CO_2 is simulated in WRF-Chem as a passive tracer. The transport of CO_2 is driven by the simulated atmospheric dynamics. Previous studies (Bakwin et al., 2004; Parazoo et al., 2008) have used the scalar conservation equation:

$$\underbrace{\frac{\partial C}{\partial t}}_{i} + \underbrace{\frac{RT}{p}\frac{F_c}{z_1}}_{ii} + \underbrace{K_m\frac{\partial^2 C}{\partial z^2}}_{iii} + \underbrace{w\frac{\partial c}{\partial z}}_{iv} + \underbrace{\overrightarrow{V_H}\cdot\nabla_H C}_{v} + \underbrace{g\frac{M\partial C}{\partial p}}_{vi} = 0 \tag{1}$$

to quantify CO_2 transport in the atmosphere where C is the CO_2 mole fractions in ppm, F_c is the surface flux of CO_2, z_1 is the lowest model level, R is the gas constant, T is temperature, p is pressure, K_m is the vertical eddy diffusivity coefficient, w is vertical velocity, $\overrightarrow{V_H}$ is horizontal velocity, g is gravity and M is the parameterized convective mass transport.

The individual terms represent the tendency in CO_2 mole fractions (i), influence of surface fluxes (ii), and transport by vertical diffusion (iii), vertical advection (iv), horizontal advection (v), and cloud convection (vi).

Term (ii) acts only on the lowest model layer. The cloud convective transport term is suitable for a model with parameterized convection. In the 3-km simulation, the convective transport is not separable from the grid-scale vertical advection and thus, in eq. 2, the term (vii) includes the vertical transport due to convection (vi) and vertical advection (iv) in eq. 1. We use lower-case c to indicate the differences. We continue to refer to term (vii) as vertical advection for simplicity Thus, at elevated model level (above the first level), the equation for high resolution models can be further reduced to:

$$\underbrace{\frac{\partial C}{\partial t}}_{i} + \underbrace{K_m\frac{\partial^2 C}{\partial z^2}}_{iii} + \underbrace{w\frac{\partial c}{\partial z}}_{vii} + \underbrace{\overrightarrow{V_H}\cdot\nabla_H C}_{v} = 0 \tag{2}$$

In our study, we consider horizontal advection, vertical advection and vertical diffusion are the transport terms representing change in CO_2 mole fractions in the atmosphere. We study the impact of these terms on the distribution of CO_2 along a frontal

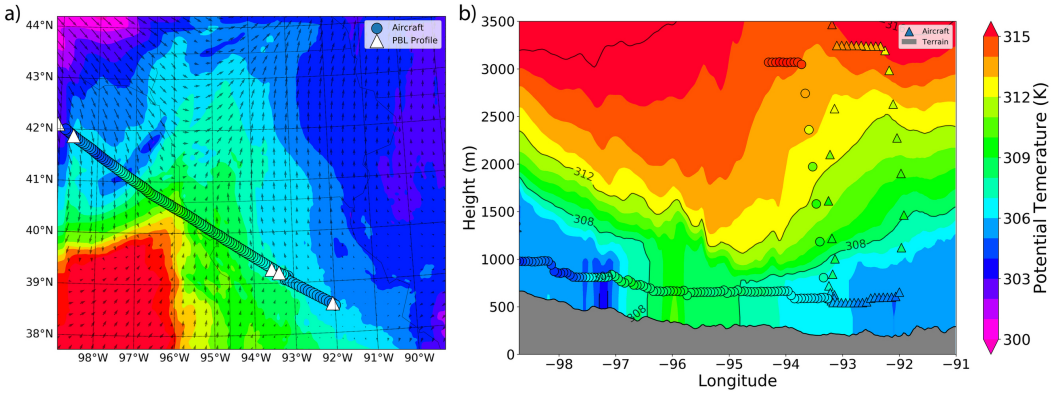

Figure 3. Comparisons of aircraft measurements to the high-resolution (3km) WRF-Chem simulation (at 548 m AGL) of potential temperature on August 4th, 2016 at 18Z. The aircraft measurements are shown as circles. Panel (a) shows simulated potential temperature overlaid with aircraft observations from approximately the same altitude, and (b) shows the vertical cross-section across the frontal boundary along the path traced by the aircraft transects. To match times with WRF-Chem outputs, aircraft measurements within ± 30 minutes of 18Z are shown.

boundary. Terms from eq. (2) were calculated using 3D velocities, CO_2 mole fractions and eddy diffusivity from WRF-Chem hourly outputs.

4 Results

4.1 Comparison to ACT-America Aircraft Measurements

WRF-Chem simulated a cold front with thermal features that are consistent with the aircraft measurements. Figure 3 shows the horizontal map and vertical cross-section of potential temperature from WRF-Chem and aircraft measurements. In figure 3(a) it can be seen that there is a region of warm air located in the south-west of the domain and a cold air mass to the north-west of the domain. Figure 3(b) shows the variability in potential temperature in a vertical cross-section across the frontal boundary. The warm and cold air masses meet at -97° longitude at the surface. The vertical distribution of potential temperature shows that there is a band of warm air ($\theta > 307K$) extending from -97° to -94° longitude. This warm air mass was also present in the aircraft measurements.

Similar to potential temperature, WRF-Chem simulates wind speed and wind direction across the front that are largely consistent with the ACT-America aircraft observations. Figure 4(a) shows that in the ABL along the frontal boundary there is a decrease in wind at the frontal boundary as seen in the aircraft measurements and WRF-Chem; the feature is most prominent between -97° and -96° longitude and 40° and 41° latitude. In the cold sector, towards the northwest region of the domain, the higher wind speeds (>9 ms^{-1}) measured by the aircraft were also captured by WRF-Chem. Southerly winds in the warm sector have lower wind speeds (<9 ms^{-1}) in WRF-Chem as well as the aircraft measurements. WRF-Chem simulated wind speeds were found to be higher than the aircraft observations. Figure 4(b) shows that the simulated wind shift from northwesterly winds in the cold sector to southerly winds in the warm sector at the frontal boundary matches the wind shift measured by the aircraft. In the south-eastern end of the flight track, there is a region of relatively calm winds (<2 ms^{-1}) where there is a mismatch in wind direction between model and observations. However, this region is rel-

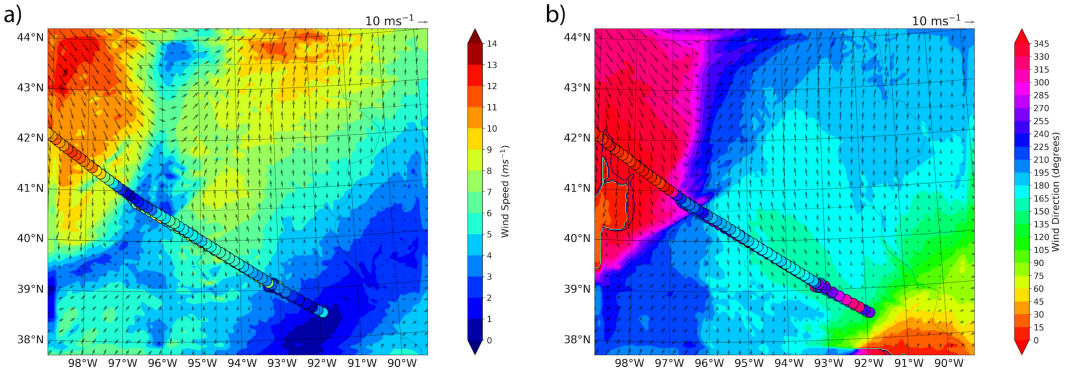

Figure 4. Comparisons of aircraft measurements to the high-resolution (3km) WRF-Chem simulation of horizontal winds on August 4th, 2016 at 18Z at an altitude of 548 m AGL. The aircraft measurements are shown as circles. Panel (a) shows the wind speed (ms-1) comparison with the WRF-Chem map overlaid with aircraft observations and panel (b) shows the wind direction (degrees) comparison with the WRF-Chem map overlaid with aircraft observations. The white triangles show the locations for the aircraft vertical profiles used to evaluate the boundary layer depth. The arrows show the wind vectors on both figures for reference.

atively far from the frontal boundary, and wind speeds are low in both the model and the observations.

Figure 3 shows the locations of the aircraft vertical profiles along the flight track where observed virtual potential temperature profiles were used to derive ABL depth and compare to the WRF-Chem diagnosed ABL depth. The WRF-Chem ABL depth was higher in the warm sector and lower in the cold sector. Table 2 summarizes the model-data differences in the warm and cold sectors. Studies conducted using similar WRF-Chem parameters have also reported values of the same order (Díaz-Isaac et al., 2018; Feng et al., 2016).

Figure 5 shows that WRF-Chem was able to represent the observed large-scale features in CO_2 mole fraction. Figure 5(a) shows simulated cross-frontal differences as high as 25 ppm. The observed frontal difference was smaller at this location. WRF-Chem did simulate the lower CO_2 mole fractions observed in the cold sector north of 41° latitude. The horizontal extent of elevated CO_2 mole fractions in the warm sector is narrower in the model as compared to the aircraft measurements. This is specifically noticeable in figure 5(b) – in WRF-Chem, the elevated concentrations extend from -96.5° to -94° longitude but in the aircraft measurements it extends from -97.7° to -93° longitude. This could be caused by a small error in the simulated location (Fig. 5(a)) of the high CO_2 region found in the model at approximately -95° longitude and 39° latitude.

There is a small region of elevated CO_2 mole fractions west of the frontal boundary into the cold sector between -98° to -97° longitude. This was seen in both aircraft measurements and WRF-Chem. Overall, WRF-Chem was able to capture the large-scale features of the CO_2 distribution at frontal boundary, including the correct sign and approximate amplitude of the cross-frontal difference. Table 2 shows the quantified statistics comparing WRF-Chem and aircraft measurements along the flight track. The distribution of CO_2 in the simulated atmosphere is determined by interactions between atmospheric transport and the surface fluxes. The misalignment of the CO_2 distribution between WRF-Chem and aircrafts can arise from errors either in transport or fluxes and detangling them to determine the cause is beyond the scope of this study. Even though the CO_2 distribution was not exactly represented as measured by the aircraft, WRF-Chem's

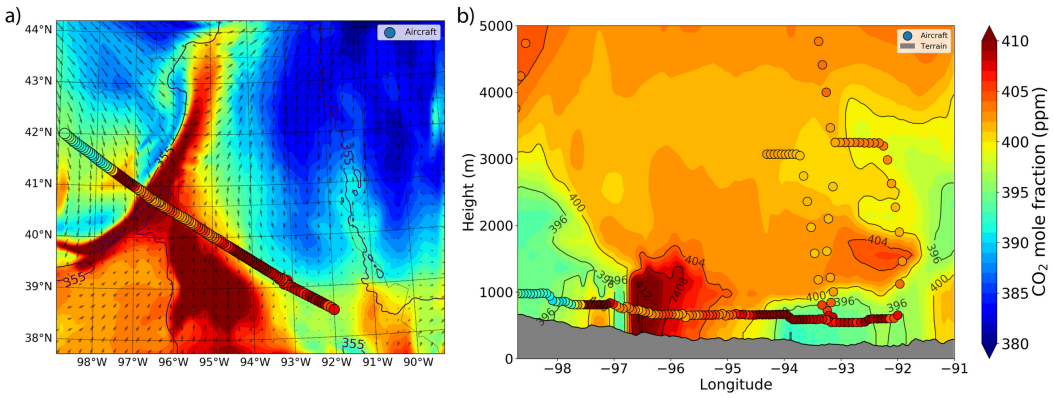

Figure 5. Comparisons of aircraft measurements to the high-resolution (3km) WRF-Chem simulation of potential temperature on August 4th, 2016 at 18Z at an altitude of 548 m AGL. The aircraft measurements are shown as circles. Panel (a) shows the horizontal map overlaid with aircraft observations. The white line shows the transect for the cross-section. Panel (b) shows the vertical cross-section across the frontal boundary highlighting the vertical features as seen by WRF-Chem and the aircraft measurements.

Table 2. Evaluation of WRF-Chem using aircraft measurements in the boundary layer. Cross-frontal differences were calculated as the difference between warm sector and cold sector values

Variable	Units	Warm Sector		Cold Sector		Cross-Frontal Difference	
		WRF	Aircraft	WRF	Aircraft	WRF	Aircraft
Potential Temperature	K	313.2	311.7	305.4	307.2	7.8	4.5
Wind Speed	ms^{-1}	6.4	5.92	12.1	10.05	-5.7	-4.13
Wind Direction	degrees	242.9	259.96	310.75	308.71	-67.85	-48.75
PBL Depth	m AGL	836.4	770	692.6	705	143.8	65
CO_2 Mole Fraction	ppm	409.6	406.4	395.9	394.7	13.8	11.7

performance in simulating the large-scale CO_2 features during the frontal passage as well as meteorological variability allows it to qualify as a platform to study CO_2 transport.

4.2 Synoptic-scale weather and CO_2 distributions on August 4^{th}

In this study, WRF-Chem simulation of CO_2 distributions during the cold front passage show the presence of a narrow band of elevated mole fractions aligned with frontal boundary.

Figure 6 shows the distribution of equivalent potential temperature (θ_e) within the innermost simulation domain at an elevation of 548m AGL at 00Z on August 5th. The frontal location was determined by the maximum gradient in θ_e in the innermost high-resolution domain (Pauluis et al., 2008). In figure 6(a), based on the contours of θ_e we can see that the cold front extends from the border of Minnesota and Wisconsin in the north to Kansas in the south. The maximum gradient is located between -94° longitude and -97° longitude between the 41° latitude and 42° latitude. Based on the gradients in θ_e across the domain, we defined the frontal boundary as the contour line corresponding to a θ_e value of 355 K, which is highlighted in figure 6(b) as the single black contour line. In addition to θ_e, the locations of the warm and cold sectors of the front are further confirmed by the changing wind directions as seen in figures 6(a) and 6(b). The cold

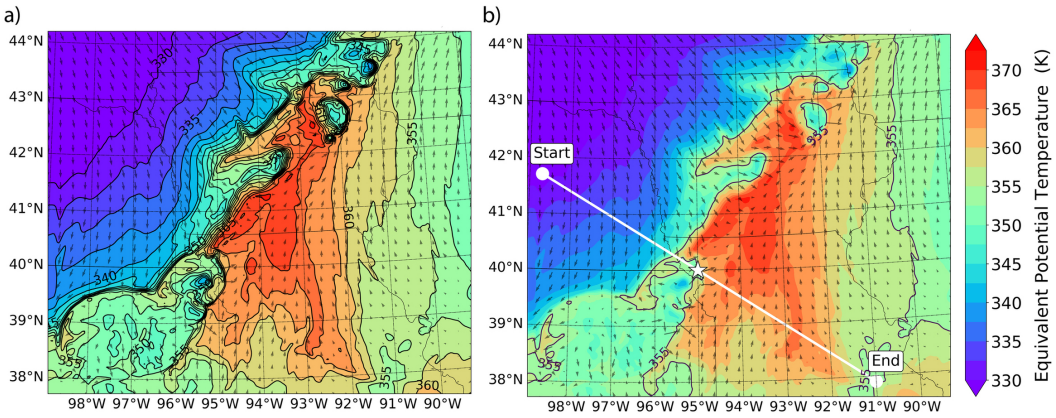

Figure 6. Map of equivalent potential temperature (θ_e) at an elevation of 548m (AGL) at 00Z on Aug 5th as simulated by WRF-Chem. Panel (a) shows the equivalent potential temperature distribution with contours used to determine the threshold value. Panel (b) shows the contour of equivalent potential temperature threshold value ($\theta_e = 355K$) highlighting the location of the front. The white line shows the transect used to study features across the frontal boundary in the warm and cold sector of the front. The star shows the location of the reference point chosen for analysis in this study.

sector has predominantly north-westerly flow covering most of Nebraska, including Lincoln, while Missouri and parts of Kansas and Iowa experience southerly winds in the warm sector. Figure 6(b) also shows a pin-wheel shape in the wind vectors at about 39° latitude, -97.5° longitude, suggestive of a convective storm located over that region.

The response of simulated CO_2 mole fractions to the cold front over continental North America can be seen in Figure 7(a). The continental scale distribution of CO_2 shows the strong gradient along the frontal boundary. In the cold sector, air with lower CO_2 mole-fractions (390 ppm) are introduced with northwesterly winds coming in from Canada. The warm sector of the front is characterized with southerly flow bringing in air with higher CO_2 mole fractions (405-410 ppm). Figure 7(b), the high-resolution simulation, shows a "zoomed-in" view of the front and associated CO_2 distribution. An elongated band of air with higher CO_2 mole fractions can be seen extending along the frontal boundary. This band has a maximum width of approximately 200 km and extends from northeastern Kansas to northeastern Iowa spanning over 800 km. The white box delimits the boundaries of the innermost domain (Figure 7(b)).

We select the line extending across the front into the warm and cold sectors and a fixed-point location, referred hereafter as our reference point, where the frontal boundary passes at 00Z (see Figure 6b) to study the vertical structure of the atmospheric CO_2 and its evolution responding to this summertime cold front (Figure 8). Figure 8(a) shows the impact of the cold front passage on CO_2 contribution at a given time across the frontal boundary. In Figure 8(a), we see the slanted structure of the front in the cold sector (western region, lower altitudes) identified by air with much lower CO_2 mole fractions (380 – 395 ppm). The CO_2 distribution is largely correlated with the alignment of θ_e contours shown as the black contours. In comparison, the warm sector has elevated CO_2 mole fractions (-94° to -95° longitude) which extend from the surface to approximately 3.5 km MSL near the frontal boundary – identified as the band of high CO_2 along the frontal boundary.

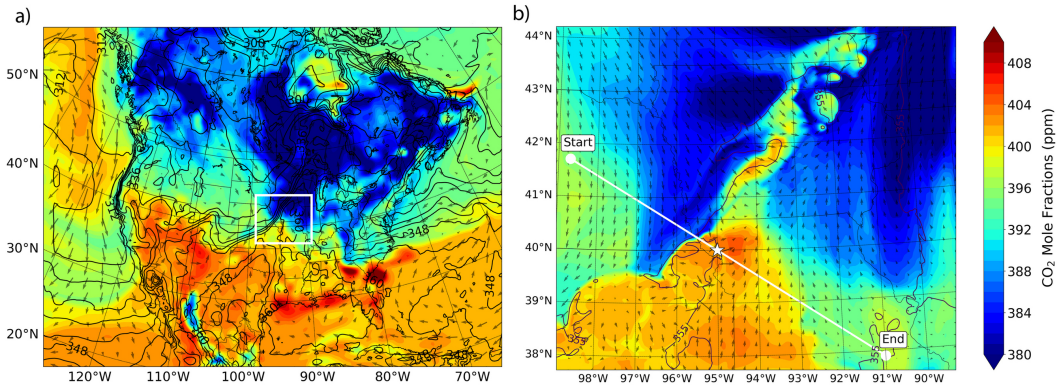

Figure 7. Maps of simulated CO_2 mole fraction on August 5th at 00Z from the outermost coarse (27km-resolution) simulation domain on the left panel (a) and the 3km grid high resolution domain on the right panel (b). The green lines show contours of equivalent potential temperature ($\theta_e = 355K$) highlighting the location of the front. Results from both domains are from 548m AGL.

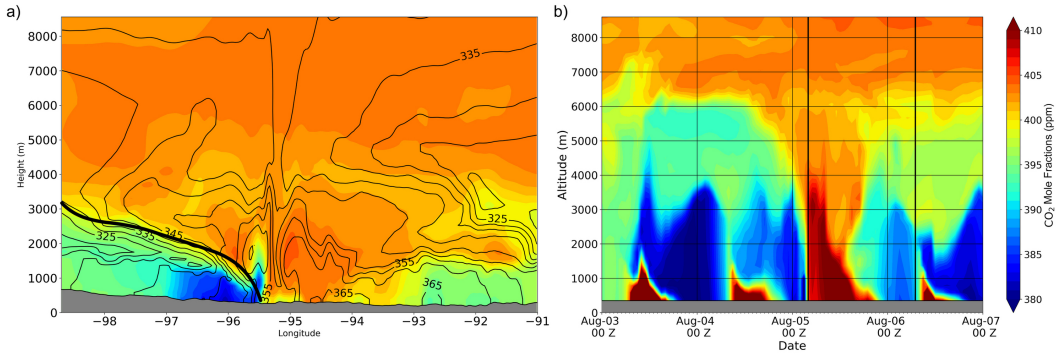

Figure 8. Vertical distribution of CO_2 during a cold front passage. (a) Vertical distribution (MSL) of CO_2 along the transect (white line in Figure 6b) shown in figure 6 highlighting the warm and cold sector of the front on August 5th at 00Z. The bold black line shows the the slanted structure of the front in the cold sector with lower CO_2 mole fractions. (b) Time evolution of CO_2 mole fractions over the reference point (white star in Figure 6b) in Nebraska from Aug 3rd to Aug 7th 00Z. The gray regions show the terrain. The vertical black lines in panel (b) show the period of frontal influence from Aug 5th 04Z to Aug 6th 09Z over the reference location.

In order to track the influence of the cold front passage on local CO_2 distribution, a time-series of vertical distribution at the reference point is shown in figure 8(b). The location experiences elevated CO_2 mole fractions between August 5th at 00Z and 18Z when the cold front passes. We also see that there are repeated periods of low CO_2 mole fractions that are centered around 00Z – these are caused by the daily cycle of ecosystem fluxes and ABL mixing. Between 00Z Aug 5th and 00Z Aug 6th, there is a period of elevated CO_2 mole fractions that is relatively uniform in the vertical, extending above 6km MSL. During this period, air mass with pre-existing gradients are being advected over the location - these gradients do not represent downward movement of air from higher up in the atmosphere. From Aug 5th 00Z, air mass over the reference location has low CO_2 mole fractions in the vertical (< 390ppm). This continues for a few more hours till 04Z when there is a sharp change in the vertical distribution of CO_2, with elevated CO_2 mole fractions (> 400ppm) extending from the surface till 6km MSL. The change in the vertical distribution of CO_2 corresponds to the change in air mass due to the frontal boundary passing over the location. The air mass with elevated CO_2 concentrations correspond to the warm sector of the front, lasting until Aug 6th 05Z. The warm sector air mass is followed by the cold sector air mass over the location with lower CO_2 mole fractions ($<$ 390ppm). This can be seen in figure 8(b) between Aug 6th 00Z and 09Z. The impact of the frontal passage over the location disrupts the repeated diurnal variation features (seen prior to Aug 5th 00Z). The components of CO_2 as well as the transport mechanisms responsible for these features are described in greater detail in sections 4.3 and 4.4 respectively.

4.3 CO_2 transport from various sources

We find that CO_2 introduced into the domain via boundary conditions along with influences from biogenic and fossil fuel components within the domain determine the distribution of CO_2 along the frontal boundary. The cross-frontal difference (calculated near the surface at -95° longitude on August 5th at 00Z in figure 8(a)) in CO_2 mole fractions is similarly influenced by these components. Figure 9 shows the distribution and time-evolution of CO_2 mole fractions for each separate component from different perspectives. Based on the horizontal maps, at 00Z on Aug 5th, strong negative biogenic CO_2 fluxes (approximately -10 ppm) between -97° and -95° longitude and 40° and 42° latitude are co-located with the cold sector air mass with low CO_2 mole fractions as seen previously in figure 7(b). In the warm sector (between -96° and -94° longitude and 41° and 39° latitude), biogenic fluxes have near zero magnitudes and are aligned with air mass with elevated CO_2 mole fractions in figure 7(b). Figure 9 shows fossil fuel fluxes have elevated mole fraction in the eastern half (between -92° and -90° longitude) of the domain. The presence of stronger negative biogenic fluxes over the same region cancels out the impact of the elevated fossil fuel mole fractions. The frontal difference is visible in the horizontal map of boundary inflow CO_2. However the magnitude of the difference is lower (2-3 ppm) when compared to the total CO_2 distribution (20-25 ppm). Biogenic fluxes show a frontal difference of 13 ppm while the fossil fuel fluxes show a frontal difference of 4 ppm. These features are further discussed and differentiated by Pal et al. (2020).

The cross-frontal difference in CO_2 mole fractions is shown in figure 9 (panels (d) to (e)). The slanted vertical structure of the cold front seen in figure 8(a) is highly correlated with boundary condition CO_2 mole fractions. The cross-frontal CO_2 difference caused by boundary conditions was around 5 ppm near the surface. The boundary inflow does not contribute to the elevated band of CO_2 along the frontal boundary. The narrow band of elevated CO_2 (2-6 ppm increase) is located near the frontal boundary from the surface to 3.5 km MSL, and between -96° and -95° longitude. This band of elevated CO_2, as well as the relatively lower near surface CO_2 mole fractions between -93° and -91° longitude are primarily influenced by biogenic CO_2 mole fractions. In figure 9(e), we see that fossil fuel has a positive contribution (2-4 ppm) near the frontal boundary (between -96° and -94° longitude), and that fossil CO_2 emissions are counteracted

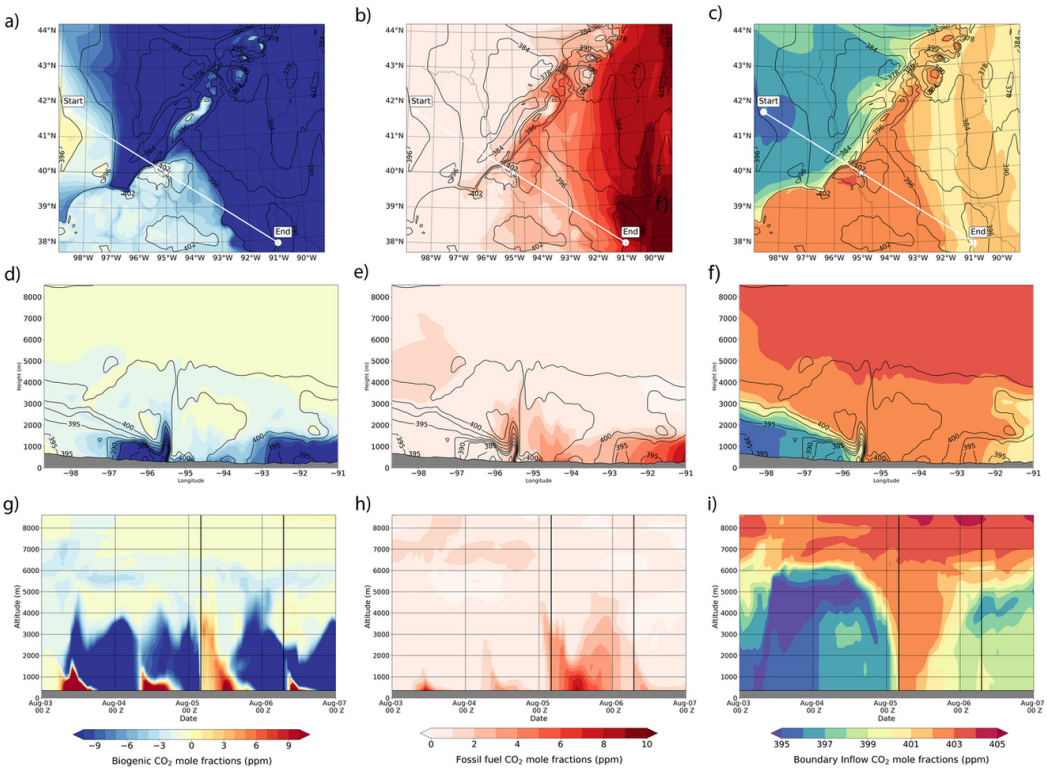

Figure 9. Distribution of CO_2 from various sources in WRF-Chem for the August 4th cold front passage. Panels (a) to (c) show a map of CO_2 from fossil fuel emissions within the domain, biospheric fluxes within the domain, and inflow of CO_2 from the domain boundaries on August 5th 00Z at an altitude of 548m AGL. Panels (d) to (f) show the vertical cross-sections along the transect (white line in panels (a) through (d)) on August 5th at 00Z. Panels (g) to (i) show the time-evolution of CO_2 from various sources over Lincoln, NE from August 3rd to August 7th at 00 UTC. The black contours of total CO_2 mole fractions are shown in panels (a) to (f).

by the strong biogenic CO_2 drawdown in the lower atmosphere between -93° and -91° longitude - further confirming that the elevated CO_2 mole fractions from fossil fuel are not a major driver of frontal CO_2 gradients.

The time-evolution analysis of various components of CO_2 shows that during the period of frontal passage, there are changes in the near surface CO_2 mole fractions driven by biogenic sources followed by fossil fuel sources acting on CO_2 advected in by boundary inflow. Variability in the vertical profile of total CO_2 mole fractions are shown in figure 9(g). Diurnal net photosynthesis and deep ABL mixing can be seen as the repeating low CO_2 mole fractions extending into the lower troposphere, coupled with nocturnal respiration causing high CO_2 mole fractions near the surface. This pattern is disrupted on August 5th at 00Z, as elevated CO_2 mole fractions are present in the atmosphere above the reference point. The difference in near surface CO_2 mole fractions between the prefrontal and frontal periods is 25 ppm. The elevated CO_2 mole fractions persist over the region for a day followed by a shorter period of depleted CO_2 mole fractions. The diurnal pattern resumes around 10Z on August 6th. This disruption to the diurnal pattern and the consequent change in the vertical distribution of CO_2 over the location is attributed to the cold front passage. From the fossil fuel mole fractions shown in figure 9(h), the only significant positive influence (between 4 ppm to 6 ppm) in mole fractions

exists between Aug 5th 00Z to Aug 6th 00Z contributing to 20% of the total near surface change in CO_2 mole fractions. These positive modulations in fossil fuel CO_2 mole fractions reduce sharply towards the end of the frontal passage period after Aug 6th 09Z. The biogenic CO_2 mole fractions are responsible for the diurnal patterns (figure 9(i)) as they represent the uptake of CO_2 by photosynthesis during the day and accumulation due to respiration at night. On Aug 5th at 04Z we see that biogenic CO_2 mole fractions shift from -10 ppm to 4 ppm, coinciding with a different air-mass advected in by the frontal boundary passing over the location.

We find that boundary inflow CO_2 is responsible for roughly 20% of the pre-frontal and frontal near surface difference in CO_2 at this location. During the frontal passage, boundary CO_2 is relatively homogenous in the vertical, with mole fractions similar to upper free tropospheric values throughout the column. Boundary CO_2 also explains a roughly 3 ppm drop in lower free troposphere and ABL CO_2 after frontal passage. The primary driver of the frontal gradient is biogenic CO_2, as it explains about 60% of the total change in CO_2 within the ABL between pre-frontal and frontal conditions.

We further explore the components of CO_2 within WRF-Chem with a footprint analysis (Figure 10 (c) and (d)) showing the air mass history across the frontal gradient. Simulated particles were released at 300 m above Lincoln, NE on Aug 4th, 20Z (pre-frontal crossing) and Aug 5th, 03Z (post-frontal crossing). These particles were tracked backwards for 5 days using a Lagrangian particle dispersion model (Uliasz, 1994) and their interactions with the surface were summed to create an influence function of the air measured above Lincoln before and after the frontal crossing. From figure 10(c), we see that the cold sector ABL air at this time and location originated in the southwestern Canada, while the warm sector (figure 10(d)) air came from the south-central region to the south. The biogenic surface fluxes in figure 10(a) are averaged over 5 days and do not quantitatively reflect the impact of the diel variations in fluxes. Qualitatively, there is not a large difference in the net biological fluxes in these two upwind areas; neither back trajectory comes from the region of strong net uptake to the north and northeast of the flight path. This result is likely to be specific to this frontal case. Since fossil fuel fluxes do not have as strong a diel variability as do biogenic fluxes, the 5-day average better represents the distribution and magnitude of fluxes.

4.4 Mechanism of CO_2 transport along the frontal boundary

Horizontal and vertical advection are the primary transport terms that drive the distribution of CO_2 at the frontal boundary. We compare the three terms driving CO_2 mole fraction gradients in both vertical and horizontal directions (cf. section 2.5) as described in equation (3), which are (*i*) horizontal advection, (*ii*) vertical advection and (*iii*) vertical diffusion. Figure 11 shows the transport terms along the transect shown in figure 6(b). Since this figure represents a snapshot in time, the sign of the transport term does not reflect its influence for the period of frontal passage. Overall, horizontal advection is strongest near the frontal boundary and has a strong negative influence in the cold sector and a weaker positive influence in the warm sector. The magnitude of horizontal advection is greatest at the frontal boundary, where the CO_2 mole fraction gradient is the strongest. As seen in figure 11(a), horizontal advection has high magnitude ($\sim$ 10 ppm/hr) in the ABL at the frontal boundary. At the frontal boundary (-95.5° longitude), near surface values of horizontal advection have postive values in the warm sector and negative values of similar magnitude in the cold sector. Alternating negative and positive values can be interpreted as transport of CO_2 from a depleted region followed by an elevated CO_2 region due to changes in the direction of the CO_2 flow as the cold front propagates. Further into the warm sector (Figure 6b) of the front, there is a region of depletion caused by horizontal advection between -95° and -94° longitude followed by accumulation between -94° and -93° longitude. However, the magnitudes are not as high as those near the frontal boundary.

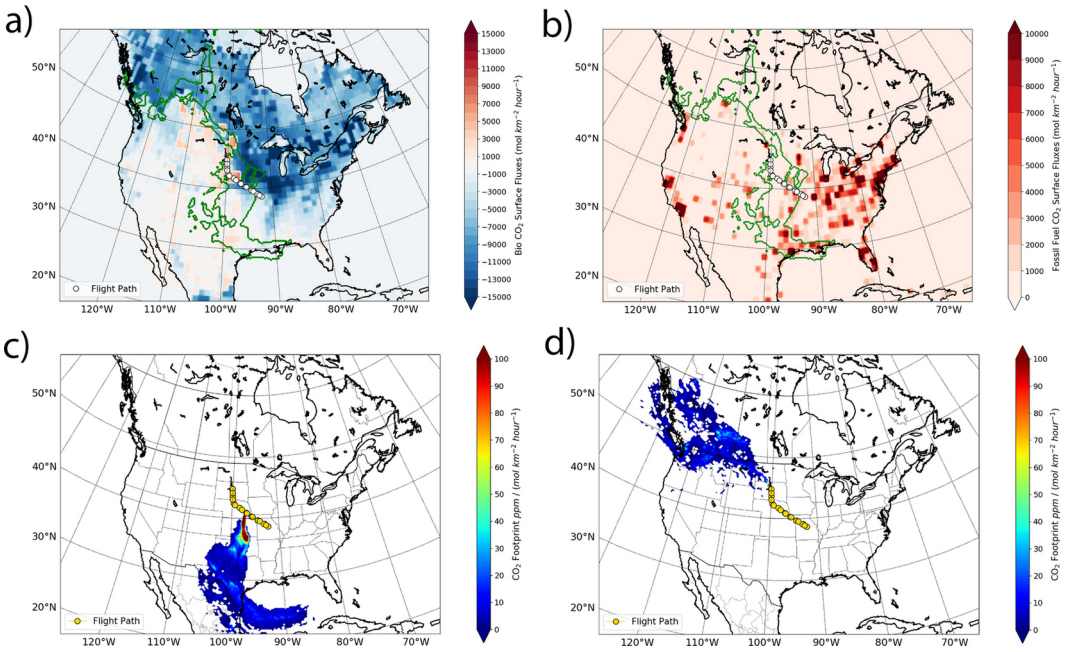

Figure 10. Footprint analysis of airmass along the frontal boundary showing the surface fluxes from CarbonTracker (CT-NRTv2017x) and regions of influence. Panel(a) has biogenic CO_2 surface fluxes and panel (b) shows fossil fuel CO_2 surface fluxes. The surface flux maps have been averaged over 5 days. Panel (c) shows the airmass history for the warm air mass ahead of the front and panel (c) shows the airmass history for the cold air mass behind the front. The flight path is shows as yellow circles.

The influence of vertical advection on the distribution of CO_2 across the front is generally restricted to the region close to the frontal boundary (between -96° and -95° longitude) as seen in figure 11(b). However, unlike horizontal advection the magnitude of vertical advection drops sharply on moving away from the frontal boundary. Vertical diffusion has a lower magnitude as well as region of influence compared to the other terms. As shown in figure 11(c), maximum values are located at the frontal boundary (at -95.5° longitude). Vertical diffusion is responsible for some near surface accumulation around the frontal boundary and depletion in the cold sector. Thus, for this cold front passage, horizontal and vertical advection play the dominant role. It is also notable that only the vertical advection term at the frontal boundary has a magnitude similar to those found in the ABL. Horizontal advection is present throughout the lower free troposphere, but reduced in magnitude when compared to the ABL.

Evolution of the vertical distribution of transport budget terms over a location shows that the terms have the greatest magnitude at the beginning of frontal influence and at the frontal boundary between the warm and cold sectors. In figure 12(a), the vertical distribution of horizontal advection over the reference location is shown from August 3rd to August 7th 00Z. At the start of the frontal influence around Aug 5th 04Z, there is a sharp increase in the magnitude of horizontal advection with negative influence in the boundary layer (-10 ppm/hr). Between 2km to 3km MSL there is a positive (10 ppm/hr) region. The abrupt change in signs near Aug 5th 04Z can be attributed to the change in air masses due to introduction of the warm sector (Figure (11c)) over the region. Simultaneously, the distribution of vertical advection is shown in figure 12(b). Unlike horizontal advection, vertical advection does not show near surface influences during the prefrontal period (apart from the nocturnal buildup). During the initial period of frontal influence, vertical advection has minimal influence under 1km MSL. The distribution above 1km MSL is similar to horizontal advection with the opposite sign. The frontal boundary separating the warm and cold sectors passes over the location around Aug 5th 12 Z and vertical and horizontal advection have similar structures with opposing signs. In these overlap regions as seen in figure 12 (a) and (b), horizontal advection has a strong depleting influence while vertical advection is resposible for the accumulation of CO_2 mole fractions. The evolution of CO_2 mole fractions in the atmosphere are shown in figure 8(b). The vertical distribution of horizontal advection and vertical advection are co-located - the warm sector of the front experiences predominantly positive influence from vertical advection over the reference location. This also corresponds to regions of elevated CO_2 mole fractions as seen in figure 8(b). Dynamically speaking, vertical advection lifts air mass with elevated CO_2 to regions with lower CO_2 mole fractions, thereby causing accumulation in the vertical. Horizontal advection carries this air mass with increased CO_2 mole fractions into air with lower mole fractions and depletes the combined CO_2 mole fractions. As the frontal boundary passes over the location (between 08Z and 12Z on Aug 5th), horizontal advection has a positive influence accumulating CO_2 near the surface. Vertical advection has a positive influence immediately after this, while horizontal advection has a negative influence. The accumulation of CO_2 near the surface is now redistributed vertically by advection into regions with depleted mole fractions (hence the positive influence). This vertical redistribution lowers the CO_2 mole fractions in the air mass to its surroundings (in the horizontal only) causing horizontal advection to have a depleting impact. This causes the opposing signs for horizontal and vertical advection. This coupled transport between horizontal and vertical advection is clearly seen during the period of frontal transport.

Vertical diffusion shows a repeated pattern throughout the period from Aug 3rd 00Z to Aug 7th 00Z. From figure 12(c) we see that there is a strong positive influence at the surface corresponding to night-time accumulation of CO_2 due to a shallow boundary layer (extending from 00Z to 09Z each day). Also, there is a large couplet of diffusion at the residual ABL top that is attributed to turbulence acting on the residual gradient in CO_2. This is then followed by depletion during the daytime (10Z to 19 or 20

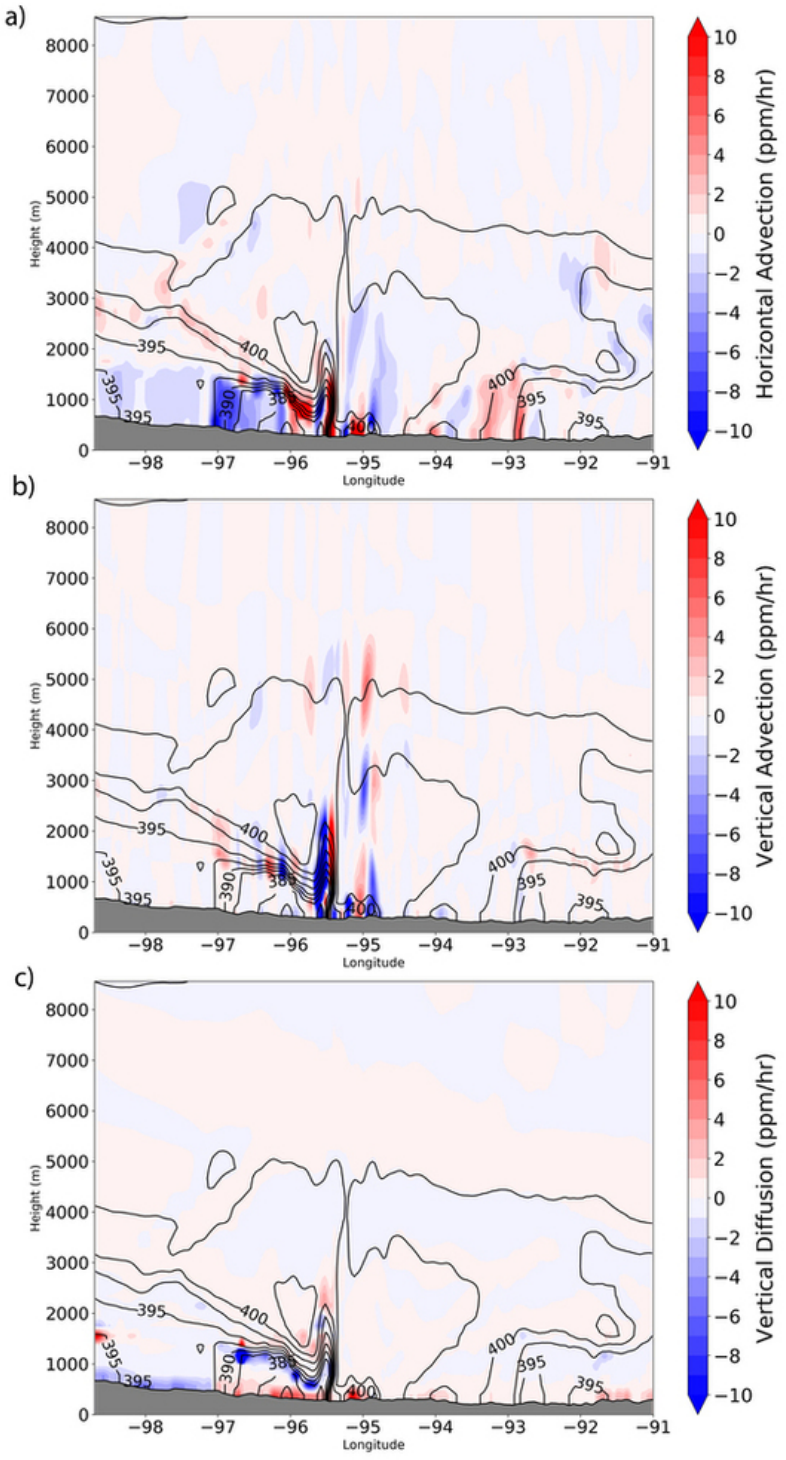

Figure 11. Transport processes impacting CO_2 distribution across the frontal boundary on August 5th at 04Z along the transect shown in figure 6(b). The colored contours show the transport terms while the black contour lines represent the corresponding CO_2 mole fractions. Panel (a) shows horizontal advection, panel (b) shows vertical advection and panel (c) shows vertical diffusion.

Z). During the passage of the frontal boundary over the location (bold lines on figure 12(c)), there are small periods of influence between 2km MSL and 4km MSL between 04Z and 12 Z on Aug 5th.

In summary, advective transport terms have a greater response to the frontal passage compared to the diffusion term. For horizontal advection and vertical advection, the impact during frontal passages differ from non-frontal periods. In comparison, vertical diffusion is not affected by the cold front passage. Based on the sign of the terms as well the region and period of influence, horizontal and vertical advection show a coupled transport impact during the frontal passage period. Vertical diffusion shows a diurnal pattern that is not modified by the frontal transport. However, it is responsible for accumulation and depletion in the ABL.

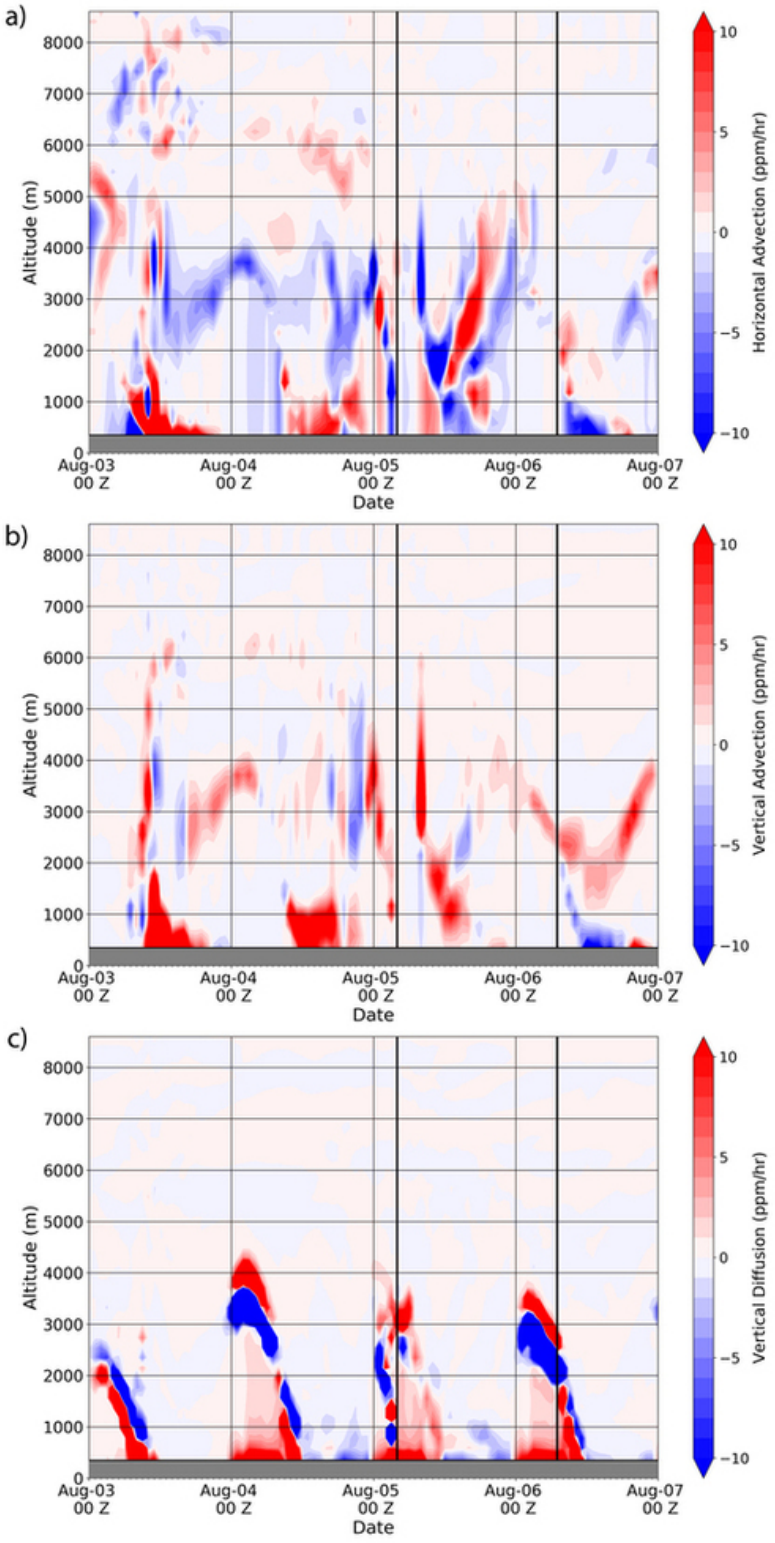

Figure 12. Evolutions of transport terms impacting CO_2 distribution across the frontal boundary from August 3rd to August 7th at 00Z over the reference location in Nebraska as shown in figure 6(b). The vertical black lines show the period of frontal influence from Aug 5th 04Z to Aug 6th 07 Z over the reference point. Panel (a) shows horizontal advection, panel (b) shows vertical advection and panel (c) shows vertical diffusion.

4.5 Discussion and conclusions

In order to understand the distribution of atmospheric CO_2 along a frontal boundary, we need to decompose the atmospheric concentrations into various sources (biogenic, fossil fuel etc.) and identify the transport mechanisms responsible. This study consisted of numerical simulations of a summer cold front passage on August 4th and 5th, 2016 over Lincoln, NE using WRF-Chem coupled with CO_2 tracers from CarbonTracker. Aircraft measurements from the NASA ACT-America 2016 campaign identified the presence of the frontal boundary and a strong gradient in CO_2 (30 ppm) near the frontal boundary.

Previous studies have also studied the impacts of frontal passages on atmospheric CO_2 distribution. Chan et al. (2004) has shown that mesoscale processes can cause variations in atmospheric CO_2 mole fractions in the range of 5 ppm to 10 ppm over the course of a day. They also reported that horizontal and vertical CO_2 transport processes influence CO_2 distributions to a similar extent as local biospheric sources. In our study, we were able to confirm these findings for the cold front passage on Aug 4th. By decomposing the CO_2 mole fractions in the atmosphere into biogenic, fossil fuel and boundary inflow contributions, we were able to highlight how local biogenic sources combined with boundary inflow were the dominant drivers. The transport equation quantified the impact of horizontal and vertical advection on CO_2 distribution along the frontal boundary. The relationship between synoptic scale horizontal transport and local vertical mixing of CO_2 has been explored in Geels et al. (2004) and the authors suggested that these motions should be resolved in numerical models. Similarly, numerical simulations with high horizontal and vertical resolution have been recommended by Geels et al. (2007) in order to capture the vertical mixing of CO_2 in the boundary layer. We use WRF-Chem with a maximum horizontal grid resolution of 3km over the target region as shown in Figure 2, and the first model level above surface is 8m AGL. Thus, the setup of WRF-Chem used is capable of capturing horizontal and vertical transport of CO_2 near the frontal boundary. By applying the CO_2 transport equation (eq. 1) Parazoo et al. (2008) have shown that for mid-latitudes, the regional gradients in atmospheric CO_2 mole fractions are caused by the horizontal advection of pre-existing upstream gradients. We were able to show the importance of horizontal advection in shaping atmospheric CO_2 mole fractions for a single cold front passage. The magnitude of the transport terms were found to be greater in our study especially near the frontal boundary (5 - 10 times).

Based on the previous paragraph, our study was able to confirm the hypothesis of previous studies. Further, we highlight the main conclusions and recommendations for future studies from our study on CO_2 distribution, origins, and transport along a frontal boundary for the August 4th cold front passage as follows:

1. An elongated band of elevated ($>$ 390 ppm) CO_2 mole fractions along the frontal boundary has been shown using high-resolution WRF-Chem simulations. This band has not been highlighted in previous studies. This band was captured in aircraft measurements as a part of the ACT-America flight campaign as well (Pal et al., 2020; Davis et al., 2018). Future work can expand on the role of this feature in determining the continental scale transport of CO_2
2. Through the use of a Lagrangian particle dispersion model, the footprint analysis showed that the air-mass corresponding to warm sector of the Aug 4th front originated over Gulf of Mexico and Texas. Similarly, the air-mass over the cold sector originated over the northwestern forests of North America. Further work can be performed by applying similar techniques to the elongated band of CO_2.
3. We found that CO_2 introduced into our domain by horizontal advection as boundary inflow had pre-existing horizontal and vertical gradients along the frontal boundary. These gradients were weaker than those observed near the frontal boundary.

Our study quantitatively showed that combining local biogenic and fossil fuel CO_2 mole fractions to the boundary CO_2 resulted in gradients similar to observations.

4. At a cloud-resolving resolution of 3km, our study was able to capture the vertical transport of CO_2 at the frontal boundary in greater detail compared to previous studies. Near the frontal boundary, where the gradients in CO_2 are strongest, horizontal and vertical advection have comparable magnitudes. We found coupled transport of CO_2 that is present only during the period frontal passage, which were quantified using the CO_2 transport equation.

A caveat of this study was that it was limited to only one frontal passage event and thus, a general theory on the impact of fronts cannot be established. Future work should be able to incorporate multiple frontal passages over a region. The presence of the elongated band of CO_2 along the frontal boundary can be tested for multiple events. Repeatable patterns of horizontal and vertical transport as seen in this case can be tested and quantified.

Acknowledgments

Primary funding for this research was provided by NASA's Earth Sciences Division as part of the Atmospheric Carbon and Transport (ACT)-America Earth Venture Suborbital mission (grant NNX15AG76G to Penn State). ACT-America aircraft datasets for this research are available at Oak Ridge National Laboratory DAAC (Davis et al., 2018). We thank M. P. Butler at the Pennsylvania State University for generating the codes that incorporate the global modeled CO_2 mole fractions into the regional model with the conservation of mass (Lauvaux, 2020). CarbonTracker (CT-NRTv2017x) results were provided by NOAA ESRL, Boulder, Colorado, United States, from the website at http://carbontracker.noaa.gov.

Computing resources were provided by the NASA High-End Computing (HEC) Program through the NASA Advanced Supercomputing (NAS) Division at Ames Research Center. The WRF-Chem model output used for this study is available at datacommons.psu.edu.

References

Bakwin, P. S., Davis, K. J., Yi, C., Wofsy, S. C., Munger, J. W., Haszpra, L., & Barcza, Z. (2004, 1). Regional carbon dioxide fluxes from mixing ratio data. *Tellus B: Chemical and Physical Meteorology*, *56*(4), 301–311. Retrieved from `https://www.tandfonline.com/doi/full/10.3402/tellusb.v56i4.16446` doi: 10.3402/tellusb.v56i4.16446

Berrisford, P., Kållberg, P., Kobayashi, S., Dee, D., Uppala, S., Simmons, A. J., ... Sato, H. (2011). Atmospheric conservation properties in ERA-Interim. *Quarterly Journal of the Royal Meteorological Society*, *137*(659), 1381–1399. Retrieved from `http://dx.doi.org/10.1002/qj.864` doi: 10.1002/qj.864

Butler, M. P., Feng, S., Bowman, K. W., Liu, J., Davis, K. J., & Lauvaux, T. (2019). Mass-conserving coupling of total column CO₂ (XCO₂) from global to mesoscale models: Case study with CMS-Flux inversion system and WRF-Chem (v3.6.1). *Geoscientific Model Development Discussions*, *2*(February), 1–35. doi: 10.5194/gmd-2018-342

Carvalho, D., Rocha, A., Gómez-Gesteira, M., & Silva Santos, C. (2014). Comparison of reanalyzed, analyzed, satellite-retrieved and NWP modelled winds with buoy data along the Iberian Peninsula coast. *Remote Sensing of Environment*, *152*, 480–492. doi: 10.1016/j.rse.2014.07.017

Chan, D., Yuen, C. W., Higuchi, K., Shashkov, A., Liu, J., Chen, J., & Worthy, D. (2004, 1). On the CO 2 exchange between the atmosphere and the biosphere: the role of synoptic and mesoscale processes. *Tellus B:*

Chemical and Physical Meteorology, *56*(3), 194–212. Retrieved from https://www.tandfonline.com/doi/full/10.3402/tellusb.v56i3.16424 doi: 10.3402/tellusb.v56i3.16424

Chen, F., & Dudhia, J. (2001). Coupling an Advanced Land Surface–Hydrology Model with the Penn State–NCAR MM5 Modeling System. Part I: Model Implementation and Sensitivity. *Monthly Weather Review*, *129*(4), 569–585. Retrieved from http://dx.doi.org/10.1175/1520-0493(2001)129%3C0569:CAALSH%3E2.0.CO%5Cn2 doi: 10.1175/1520-0493(2001)129⟨0569:CAALSH⟩2.0.CO;2

Corbin, K. D., & Denning, A. S. (2006). Using continuous data to estimate clear-sky errors in inversions of satellite Co2 measurements. *Geophysical Research Letters*, *33*(12), 4–7. doi: 10.1029/2006GL025910

Davis, K. J., Obland, M. D., Lin, B., Lauvaux, T., O'Dell, C. W., Meadows, B., ... Nehrir, A. R. (2018). *ACT-America: L3 Merged In Situ Atmospheric Trace Gases and Flask Data, Eastern USA.* ORNL Distributed Active Archive Center. Retrieved from https://daac.ornl.gov/cgi-bin/dsviewer.pl?ds_id=1593 doi: 10.3334/ORNLDAAC/1593

Dee, D. P., Uppala, S. M., Simmons, A. J., Berrisford, P., Poli, P., Kobayashi, S., ... Vitart, F. (2011, 4). The ERA-Interim reanalysis: configuration and performance of the data assimilation system. *Quarterly Journal of the Royal Meteorological Society*, *137*(656), 553–597. Retrieved from http://doi.wiley.com/10.1002/qj.828 doi: 10.1002/qj.828

Denning, a. S., Fung, I. Y., & Randall, D. (1995). *Latitudinal gradient of atmospheric CO2 due to seasonal exchange with land biota* (Vol. 376) (No. 6537). doi: 10.1038/376240a0

Díaz-Isaac, L. I., Lauvaux, T., & Davis, K. J. (2018, 10). Impact of physical parameterizations and initial conditions on simulated atmospheric transport and CO ¡sub¿2¡/sub¿ mole fractions in the US Midwest. *Atmospheric Chemistry and Physics*, *18*(20), 14813–14835. Retrieved from https://www.atmos-chem-phys.net/18/14813/2018/ doi: 10.5194/acp-18-14813-2018

Digangi, J. P., Choi, Y., Nowak, J. B., Halliday, H. S., & Yang, M. M. (2018). *ACT-America: L2 In Situ Atmospheric CO2, CO, CH4, and O3 Concentrations, Eastern USA.* ORNL Distributed Active Archive Center. doi: 10.3334/ORNLDAAC/1556

Edenhofer, O., Pichs-Madruga, R., Sokona, Y., Kadner, S., Minx, J. C., Brunner, S., ... Zwickel, T. (2014). Climate Change 2014 Mitigation of Climate Change. In *Working group iii contribution to the fifth assessment report of the intergovernmental panel on climate change* (p. 1454). Cambridge: Cambridge University Press. Retrieved from http://www.ipcc.ch/report/ar5/wg3/%0Ahttp://ebooks.cambridge.org/ref/id/CBO9781107415416http://ebooks.cambridge.org/ref/id/CBO9781107415416 doi: 10.1017/CBO9781107415416

Enting, I. G., Trudinger, C. M., & Francey, R. J. (1995, 2). A synthesis inversion of the concentration and delta13 C of atmospheric CO2. *Tellus B*, *47*(1-2), 35–52. doi: 10.1034/j.1600-0889.47.issue1.5.x

Feng, S., Lauvaux, T., Davis, K. J., Keller, K., Zhou, Y., Williams, C., ... Baker, I. (2019, 12). Seasonal Characteristics of Model Uncertainties From Biogenic Fluxes, Transport, and Large-Scale Boundary Inflow in Atmospheric CO2 Simulations Over North America. *Journal of Geophysical Research: Atmospheres*, *124*(24), 14325–14346. Retrieved from https://doi.org/10.1029/2019JD031165 doi: 10.1029/2019JD031165

Feng, S., Lauvaux, T., Keller, K., Davis, K. J., Rayner, P., Oda, T., & Gurney, K. R. (2019, 11). A Road Map for Improving the Treatment of Uncertainties in High-Resolution Regional Carbon Flux Inverse Estimates. *Geophysical*

Research Letters, *46*(22), 13461–13469. Retrieved from https://doi.org/10.1029/2019GL082987 doi: 10.1029/2019GL082987

Feng, S., Lauvaux, T., Newman, S., Rao, P., Ahmadov, R., Deng, A., ... Yung, Y. L. (2016). LA Megacity: a High-Resolution Land-Atmosphere Modelling System for Urban CO₂ Emissions. *Atmospheric Chemistry and Physics Discussions*(March), 1–56. Retrieved from http://www.atmos-chem-phys-discuss.net/acp-2016-143/ doi: 10.5194/acp-2016-143

Friedlingstein, P., & Prentice, I. (2010, 10). Carbon–climate feedbacks: a review of model and observation based estimates. *Current Opinion in Environmental Sustainability*, *2*(4), 251–257. Retrieved from http://www.sciencedirect.com/science/article/pii/S1877343510000473https://linkinghub.elsevier.com/retrieve/pii/S1877343510000473 doi: 10.1016/j.cosust.2010.06.002

Geels, C., Doney, S. C., Dargaville, R., Brandt, J., & Christensen, J. H. (2004, 1). Investigating the sources of synoptic variability in atmospheric CO 2 measurements over the Northern Hemisphere continents: a regional model study. *Tellus B: Chemical and Physical Meteorology*, *56*(1), 35–50. Retrieved from https://www.tandfonline.com/doi/full/10.3402/tellusb.v56i1.16399 doi: 10.3402/tellusb.v56i1.16399

Geels, C., Gloor, M., Ciais, P., Bousquet, P., Peylin, P., Vermeulen, A. T., ... Santaguida, R. (2007, 7). Comparing atmospheric transport models for future regional inversions over Europe – Part 1: mapping the atmospheric CO¡sub¿2¡/sub¿ signals. *Atmospheric Chemistry and Physics*, *7*(13), 3461–3479. Retrieved from http://www.atmos-chem-phys.net/7/3461/2007/ doi: 10.5194/acp-7-3461-2007

Gurney, K. R., Law, R. M., Denning, A. S., Rayner, P. J., Baker, D., Bousquet, P., ... Yuen, C.-W. (2002, 2). Towards robust regional estimates of CO2 sources and sinks using atmospheric transport models. *Nature*, *415*(6872), 626–630. Retrieved from https://doi.org/10.1038/415626ahttps://www.nature.com/articles/415626a#supplementary-informationhttp://www.nature.com/articles/415626a doi: 10.1038/415626a

Houghton, R. A., House, J. I., Pongratz, J., van der Werf, G. R., DeFries, R. S., Hansen, M. C., ... Ramankutty, N. (2012, 12). Carbon emissions from land use and land-cover change. *Biogeosciences*, *9*(12), 5125–5142. Retrieved from https://www.biogeosciences.net/9/5125/2012/ doi: 10.5194/bg-9-5125-2012

Houweling, S., Aben, I., Breon, F. M., Chevallier, F., Deutscher, N., Engelen, R., ... Serrar, S. (2010). The importance of transport model uncertainties for the estimation of CO2 sources and sinks using satellite measurements. *Atmospheric Chemistry and Physics*, *10*(20), 9981–9992. doi: 10.5194/acp-10-9981-2010

Huntzinger, D. N., Michalak, A. M., Schwalm, C., Ciais, P., King, A. W., Fang, Y., ... Zhao, F. (2017, 12). Uncertainty in the response of terrestrial carbon sink to environmental drivers undermines carbon-climate feedback predictions. *Scientific Reports*, *7*(1), 4765. Retrieved from http://www.nature.com/articles/s41598-017-03818-2 doi: 10.1038/s41598-017-03818-2

Hurwitz, M. D., Ricciuto, D. M., Bakwin, P. S., Davis, K. J., Wang, W., Yi, C., & Butler, M. P. (2004). Transport of Carbon Dioxide in the Presence of Storm Systems over a Northern Wisconsin Forest. *Journal of the Atmospheric Sciences*, *61*(5), 607–618. doi: 10.1175/1520-0469(2004)061⟨0607:TOCDIT⟩2.0.CO;2

Iacono, M. J., Delamere, J. S., Mlawer, E. J., Shephard, M. W., Clough, S. A., & Collins, W. D. (2008). Radiative forcing by long-lived greenhouse gases: Calculations with the AER radiative transfer models. *Journal of Geophysical Research: Atmospheres*, *113*(D13), n/a-n/a. Retrieved from

http://dx.doi.org/10.1029/2008JD009944 doi: 10.1029/2008JD009944

Kain, J. S. (2004). The Kain–Fritsch Convective Parameterization: An Update. *Journal of Applied Meteorology*, *43*(1), 170–181. Retrieved from http://journals.ametsoc.org/doi/abs/10.1175/1520-0450(2004)043%3C0170:TKCPAU%3E2.0.CO;2 doi: 10.1175/1520-0450(2004)043⟨0170:TKCPAU⟩2.0.CO;2

Kawa, S. R. (2004). Global CO 2 transport simulations using meteorological data from the NASA data assimilation system. *Journal of Geophysical Research*, *109*(D18), D18312. Retrieved from http://doi.wiley.com/10.1029/2004JD004554 doi: 10.1029/2004JD004554

Lauvaux, T. (2020, 5). *psu-inversion/WRF_boundary_coupling: WRF Boundary Coupling (Tracer mode - Chemistry).* Retrieved from https://zenodo.org/record/3832214 doi: 10.5281/ZENODO.3832214

Lauvaux, T., & Davis, K. J. (2014, 1). Planetary boundary layer errors in mesoscale inversions of column-integrated CO 2 measurements. *Journal of Geophysical Research: Atmospheres*, *119*(2), 490–508. Retrieved from http://doi.wiley.com/10.1002/2013JD020175 doi: 10.1002/2013JD020175

Lauvaux, T., Schuh, A. E., Uliasz, M., Richardson, S., Miles, N., Andrews, A. E., ... Davis, K. J. (2012, 1). Constraining the CO₂ budget of the corn belt: exploring uncertainties from the assumptions in a mesoscale inverse system. *Atmospheric Chemistry and Physics*, *12*(1), 337–354. Retrieved from https://www.atmos-chem-phys.net/12/337/2012/ doi: 10.5194/acp-12-337-2012

Law, R. M., Rayner, P. J., Denning, A. S., Erickson, D., Fung, I. Y., Heimann, M., ... Watterson, I. G. (1996). *Variations in modeled atmospheric transport of carbon dioxide and the consequences for CO 2 inversions* (Vol. 10) (No. 4). doi: 10.1029/96GB01892

Le Quéré, C., Andrew, R. M., Friedlingstein, P., Sitch, S., Pongratz, J., Manning, A. C., ... Zhu, D. (2017). Global Carbon Budget 2017 (pre-print). *Earth System Science Data Discussions*, *pre print*(November), 1–79. Retrieved from https://www.earth-syst-sci-data-discuss.net/essd-2017-123/ doi: 10.5194/essd-2017-123

Le Quéré, C., Raupach, M. R., Canadell, J. G., Marland, G., Le Quéré, C., Raupach, M. R., ... Woodward, F. I. (2009, 12). Trends in the sources and sinks of carbon dioxide. *Nature Geoscience*, *2*(12), 831–836. Retrieved from http://dx.doi.org/10.1038/ngeo689http://www.nature.com/articles/ngeo689 doi: 10.1038/ngeo689

Miles, N. L., Richardson, S. J., Davis, K. J., Lauvaux, T., Andrews, A. E., West, T. O., ... Crosson, E. R. (2012, 3). Large amplitude spatial and temporal gradients in atmospheric boundary layer CO2mole fractions detected with a tower-based network in the U.S. upper Midwest. *Journal of Geophysical Research: Biogeosciences*, *117*(G1). Retrieved from https://doi.org/10.1029/2011JG001781 doi: 10.1029/2011JG001781

Nakanishi, M., & Niino, H. (2006). An improved Mellor-Yamada Level-3 model: Its numerical stability and application to a regional prediction of advection fog. *Boundary-Layer Meteorology*, *119*(2), 397–407. doi: 10.1007/s10546-005-9030-8

Pal, S., Davis, K. J., Lauvaux, T., Browell, E. V., Gaudet, B. J., Stauffer, D. R., ... Zhang, F. (2020, 3). Observations of Greenhouse Gas Changes Across Summer Frontal Boundaries in the Eastern United States. *Journal of Geophysical Research: Atmospheres*, *125*(5), e2019JD030526. Retrieved from https://doi.org/10.1029/2019JD030526https://onlinelibrary.wiley.com/doi/abs/10.1029/2019JD030526 doi: 10.1029/2019JD030526

Parazoo, N. C., Denning, A. S., Berry, J. A., Wolf, A., Randall, D. A., Kawa, S. R., ... Doney, S. C. (2011). Moist synoptic transport of CO¡inf¿2¡/inf¿ along

the mid-latitude storm track. *Geophysical Research Letters*, *38*(9), 1–6. doi: 10.1029/2011GL047238

Parazoo, N. C., Denning, A. S., Kawa, S. R., Corbin, K. D., Lokupitiya, R. S., & Baker, I. T. (2008). Mechanisms for synoptic variations of atmospheric CO2 in North America, South America and Europe. *Atmospheric Chemistry and Physics*, *8*(23), 7239–7254. Retrieved from http://www.atmos-chem-phys.net/8/7239/2008/ doi: 10.5194/acp-8-7239-2008

Pauluis, O., Czaja, A., & Korty, R. (2008, 8). The Global Atmospheric Circulation on Moist Isentropes. *Science*, *321*(5892), 1075–1078. doi: 10.1126/science.1159649

Peters, W., Jacobson, A. R., Sweeney, C., Andrews, A. E., Conway, T. J., Masarie, K., ... Tans, P. P. (2007, 11). An atmospheric perspective on North American carbon dioxide exchange: CarbonTracker. *Proceedings of the National Academy of Sciences*, *104*(48), 18925–18930. Retrieved from http://www.pnas.org/content/104/48/18925.abstract doi: 10.1073/pnas.0708986104

Peylin, P., Baker, D., Sarmiento, J., Ciais, P., & Bousquets, P. (2002). Influence of transport uncertainty on annual mean and seasonal inversions of atmospheric CO2 data. *Journal of Geophysical Research Atmospheres*, *107*(19), 4385. Retrieved from http://doi.wiley.com/10.1029/2001JD000857 doi: 10.1029/2001JD000857

Schuh, A. E., Jacobson, A. R., Basu, S., Weir, B., Baker, D., Bowman, K., ... Palmer, P. I. (2019, 4). Quantifying the Impact of Atmospheric Transport Uncertainty on CO 2 Surface Flux Estimates. *Global Biogeochemical Cycles*, *33*(4), 484–500. doi: 10.1029/2018GB006086

Skamarock, W., Klemp, J., Dudhi, J., Gill, D., Barker, D., Duda, M., ... Powers, J. (2008). A Description of the Advanced Research WRF Version 3. *Technical Report*(June), 113. doi: 10.5065/D6DZ069T

Skeie, R. B., Berntsen, T. K., Myhre, G., Tanaka, K., Kvalevåg, M. M., & Hoyle, C. R. (2011, 11). Anthropogenic radiative forcing time series from pre-industrial times until 2010. *Atmospheric Chemistry and Physics*, *11*(22), 11827–11857. Retrieved from https://www.atmos-chem-phys.net/11/11827/2011/ doi: 10.5194/acp-11-11827-2011

Tans, P. P., Fung, I. Y., & Takahashi, T. (1990, 3). Observational Contrains on the Global Atmospheric Co₂ Budget. *Science*, *247*(4949), 1431 LP - 1438. Retrieved from http://science.sciencemag.org/content/247/4949/1431.abstract doi: 10.1126/science.247.4949.1431

Thompson, G., Field, P. R., Rasmussen, R. M., & Hall, W. D. (2008). Explicit Forecasts of Winter Precipitation Using an Improved Bulk Microphysics Scheme. Part II: Implementation of a New Snow Parameterization. *Monthly Weather Review*, *136*(12), 5095–5115. Retrieved from http://dx.doi.org/10.1175/2008MWR2387.1 doi: 10.1175/2008MWR2387.1

Uliasz, M. (1994). Lagrangian particle dispersion modeling in mesoscale applications. In *Smr* (Vol. 760, p. 23).

Xiao, J., Davis, K. J., Urban, N. M., & Keller, K. (2014, 6). Uncertainty in model parameters and regional carbon fluxes: A model-data fusion approach. *Agricultural and Forest Meteorology*, *189-190*, 175–186. Retrieved from http://dx.doi.org/10.1016/j.agrformet.2014.01.022https://linkinghub.elsevier.com/retrieve/pii/S0168192314000318 doi: 10.1016/j.agrformet.2014.01.022